J. Fluid Mech. (1988), *vol.* 197, *pp.* 429–451
Printed in Great Britain

Critical layers in accelerating two-layer flows

By DONALD B. ALTMAN
Institute for Naval Oceanography, Stennis Space Center, MS 39529, USA

(Received 13 May 1987 and in revised form 17 May 1988)

A series of laboratory experiments on accelerating two-layer shear flows over topography is described. The mean flow reverses at the interface of the layers, forcing a critical layer to occur there. It is found that for a sufficiently thin interface, a slowly growing recirculating region, the 'acceleration rotor', develops on the interfacial wave at mean-flow Richardson numbers of $O(0.5)$. This, in turn, can induce a secondary dynamical shear instability on the trailing edge of the wave. A single-mode, linear, two-layer numerical model reproduces many features of the acceleration rotor if mean-flow acceleration and bottom forcing are included. Velocity measurements are obtained from photographs using image processing software developed for the automated reading of particle-streak photographs. Typical results are shown.

1. Introduction

Understanding the varied mechanisms for momentum transfer in the interactions of internal gravity waves with mean flows is a topic of continuing interest in geophysical fluid mechanics. For example, field studies of lee waves by Armi (1978) and Stacey & Zedel (1986), laboratory work on critical layers by Thorpe (1981) and Koop & McGee (1983), along with theoretical studies by Fritts (1982) and others have demonstrated some of the widely varied phenomena associated with steady stratified flows over topography. Internal waves generated by such flows can break, either by convective instability (Haury, Briscoe & Orr 1979) or by dynamical instability (Thorpe 1981, figure 9), or can transfer their energy to the mean flow without obvious breaking (Thorpe 1981, figure 4).

Although interactions of internal waves with steady shear flows are far from understood, studies of internal waves in accelerating shear flows show additional surprising behaviour. Thorpe (1978) has shown by experiments and numerical modelling that over 80% of the energy of an internal wave can be transferred to the accelerating mean flow before breaking occurs. His numerical results indicate that breaking in accelerating flows is delayed when compared with steady mean flows. Delayed in this sense means that a lower mean-flow Richardson number is reached before breaking occurs. Thorpe (1981), in his ray-tracing solutions for critical layers in accelerating flow, showed rays crossing owing to the acceleration. This has been investigated by Broutman (1984) who demonstrated instabilities due to 'refractive convergence' in numerical models of accelerating shear flows.

In contrast to the above work, which concentrates on constant-buoyancy-frequency accelerating flows, the present work is an experimental study of internal waves in two-layer accelerating flows. In the experiments, a new scenario for convective instability, the 'acceleration rotor', will be investigated. This instability can occur at mean-flow Richardson numbers $O(0.5)$, and is shown to be a result of mean shear acceleration.

The paper is organized as follows. First, the experimental apparatus and technique are discussed. Then, in order to motivate the theory, an experiment showing the acceleration-rotor phenomenon is reviewed. Next, a simple two-layer, linear, single-mode model of the flow is developed and compared with steady-state, two-layer, linear theory and with the experiments. Features of the experiments not represented in the model, such as the finite thickness of the interface between layers are discussed. Finally, a summary of results is presented.

An Appendix describes the software developed and used for the automated reading of streak photographs.

2. Technique and experiments

The experiments are performed in a tilting tank similar to, but larger than, that of Thorpe (1968). Tank dimensions are $30.5\times30.5\times503$ cm. Easily replaceable sinusoidal false bottoms allow changes of forcing amplitude (0.64 or 1.27 cm) and wavelength (25.0 and 50.0 cm). A prototype experiment showed that sidewall effects extend approximately one half the distance to the centre of the tank.

The tank is tilted using a counterweight arrangement with automotive shock absorbers to limit angular velocity. Nominal tilt is 3.4° or 4.7° repeatable to $\pm0.03°$. Time to full tilt is 1.0 s repeatable to ±0.1 s.

The tank is filled with fresh water ($\rho = 1.000\pm0.001$ g cm^{-3}) and seawater ($\rho = 1.026\pm0.001$ g cm^{-3}), that has been filtered, temperature equilibrated, and degassed. Density profiles and fixed conductivity records are measured with a Precision Measurement Engineering† model 106 four-wire conductivity instrument, calibrated directly to water samples with a precision hydrometer. This instrument resolves conductivity to within 0.1% full scale with no appreciable drift during the course of an experiment. Spatial resolution is $O(0.2$ cm) when samples are taken at 30 to 50 Hz after 18 dB/octave analog filtering at the Nyquist frequency. A typical density profile is shown in figure 1.

Flow visualization and velocity measurements are by means of particle-streak photography. The area visualized is approximately 65×30.5 cm just 'uphill' of the tank pivot. A central strip of the tank, 3.8 cm wide, is illuminated with quartz iodine movie lights for photographs. Photographs are taken with a Hasselblad 500EL using a Zeiss 80 mm f/2.8 lens. Exposure timing is digitally recorded to within 1 ms. 16 mm movies of the experiments served as a check on flow behaviour between streak photographs. A brief description of the velocity measurements can be found in the Appendix to this paper.

All experiments have the geometry and frame of reference shown in figure 2. Two-layer stratification is created, and an accelerating, two-layer shear flow with a critical layer at the interface is initiated when the tank is tilted. The mean flow observed is similar to that sketched.

In total, thirteen runs of the experiment were performed to explore the effects of varying the acceleration, bottom topography, interface thickness, and ratio of layer thicknesses on the behaviour of the critical-layer flow. The experiments are summarized in table 1. In the table, λ is the wavelength of the bottom ripples, θ is the tank tilt, γ the ratio of upper to lower layer thicknesses, $\dot{F}_1$ a measure of lower layer acceleration, σ the steepness of the bottom ripples, δ a measure of lower-layer

---

† Precision Measurement Engineering, 732 North Highway 101, Suite E, Encinitas, California 92024.

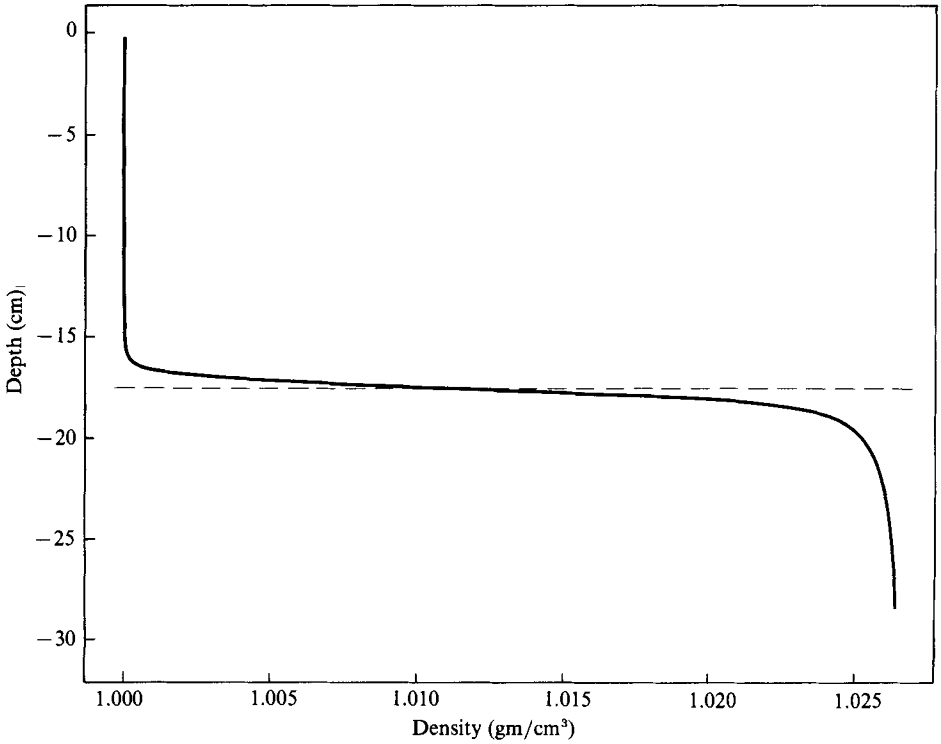

FIGURE 1. Density profile for experiment II.

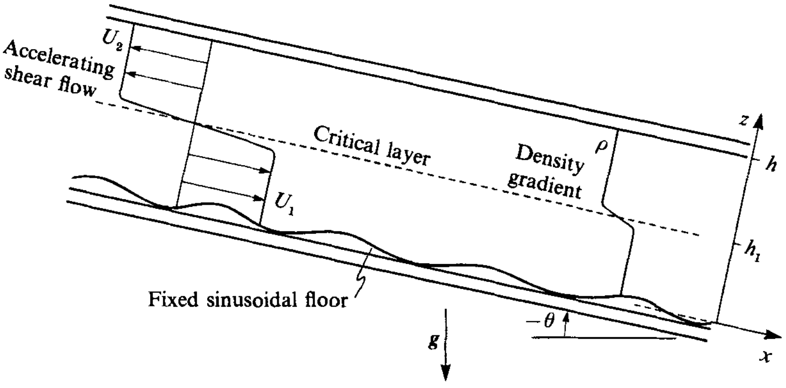

FIGURE 2. Geometry of the experiments (after Thorpe 1981).

depth, and η_i/T_i an inverse measure of interface thickness. Non-dimensional quantities are defined in the next section.

In order to clarify subsequent discussion, a typical experiment, number II of table 1, will now be discussed. Photographs are shown in figure 3. The measured density profile for this experiment is that of figure 1. Photographs are taken approximately 1.1 s apart with an exposure time of roughly 0.14 s. Frame numbers are counted from the start of the film. Tank tilt commences 0.04 s before the first frame. Photographs have been printed with the tilt removed. The interface between the two layers is delineated by a high density of particles clustered there. The horizontal line near the top of each frame is the intersection of the tank top with the rear wall. The slight

Experiment	λ(cm)	θ(degrees)	γ	$\dot{F}_1(\times 10^2)$	σ	δ	η_i/T_i
I	25.0	4.7	0.91	3.84	0.32	3.61	8.55×10^{-3}
II	25.0	4.7	1.67	5.07	0.32	2.59	2.33×10^{-2}
III	25.0	4.7	0.67	3.26	0.32	4.13	4.81×10^{-3}
IV	25.0	4.7†	1.09	4.25	0.32	3.30	1.91×10^{-2}
V	25.0	4.7†	1.13	4.28	0.32	3.24	1.38×10^{-2}
VI a	25.0	4.7	1.13	4.29	0.32	3.24	1.30×10^{-2}
b	25.0	4.7	1.13	4.29	0.32	3.24	3.66×10^{-3}
VII a	25.0	3.4	1.44	3.45	0.32	2.83	1.57×10^{-2}
b	25.0	3.4	1.44	3.45	0.32	2.83	1.16×10^{-2}
c	25.0	3.4	1.44	3.45	0.32	2.83	6.79×10^{-3}
VIII a	50.0	4.6	1.81	5.05	0.08	1.26	4.76×10^{-2}
b	50.0	4.6	1.81	5.05	0.08	1.26	1.22×10^{-2}
IX	50.0	4.6	0.47	2.51	0.08	2.40	2.04×10^{-2}
X	25.0	4.7	1.00	3.97	0.08	1.77	4.95×10^{-2}
XI	25.0	4.7	2.00	5.36	0.16	2.35	2.15×10^{-2}
XII	25.0	4.7	1.00	4.01	0.16	3.53	6.64×10^{-3}
XIII	25.0	4.7	0.50	2.66	0.16	4.71	2.05×10^{-3}

† Tilted initially, then righted.

TABLE 1. Summary of experiments

waviness of the streaks is due to a high-frequency – about 16 Hz – vibration in the truss supporting the tank.

Elapsed time is denoted by τ. *Ri* is a measured mean flow Richardson number based on average velocities away from the interface and unperturbed interface thickness. These and other non-dimensional parameters are defined in the next section.

In figure 3(*b*) ($\tau = 15.0, Ri = 0.86$) the lower layer is accelerating to the right and the upper layer to the left. The lower-layer flow is affected by the bottom, but the interface is as yet unperturbed. Rapid flow at the top of the tank is due to trapped air bubbles dislodged when the tank is tilted.

Figures 3(*d*) and 3(*e*) ($\tau = 20.5$ and 23.3, $Ri = 0.44$ and 0.33) show the slow growth of a rotor region termed the acceleration rotor. It is characterized by slowly growing regions of closed streamlines at the interface that are phase-locked to the bottom topography.

In figure 3(*f*) ($\tau = 26.1, Ri = 0.24$) the acceleration rotor continues to grow. The flow is starting to separate from the bottom causing an effective phase shift and decrease in amplitude of the bottom forcing. The separation is strikingly similar to the cases studied by Buckles, Hanratty & Adrian (1984) and Zilker & Hanratty (1979), although in their experiments the mean flow was fully turbulent and was not accelerating.

Figure 3(*h*) ($\tau = 31.6, Ri = 0.16$) shows the appearance of a secondary vortex at $X = \frac{2}{3}\pi$ to the right of each acceleration rotor. The two vortices interact in figure 3(*i*) ($\tau = 33.3$). The secondary vortex has swung over the acceleration rotor and the interaction has resulted in a region of 'cottony' texture. This is due to three-dimensional turbulent fluctuations in index of refraction sufficiently rapid compared with the shutter opening to cause a blurring of the images of individual particles. Measurements with a fixed conductivity probe along the centreline of the tank during some experiments confirm the presence here of wide-band fluctuations,

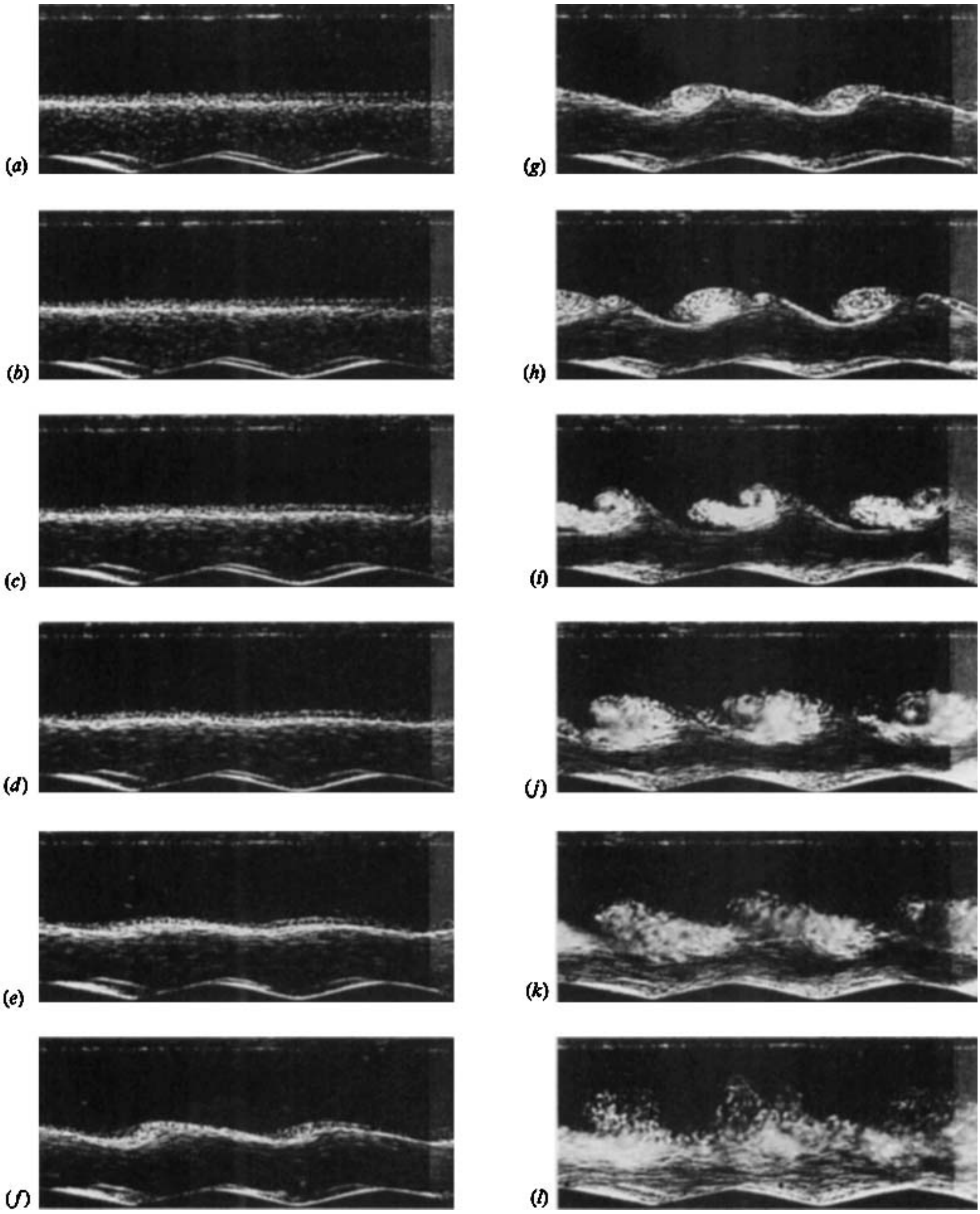

FIGURE 3. Experiment II. Pictures, with exposure times of approximately 0.25 s, are taken at τ (Ri) of (*a*) 13.177 (1.30), (*b*) 14.971 (0.86), (*c*) 17.743 (0.66), (*d*) 20.519 (0.44), (*e*) 23.280 (0.33), (*f*) 26.071 (0.24), (*g*) 28.828 (0.18), (*h*) 31.584 (0.16), (*i*) 33.300 (N/A), (*j*) 36.087 (N/A), (*k*) 38.887 (N/A), (*l*) 41.713 (N/A).

although the apparent extent of the region may be in part an artifact of sidewall effects.

In figures 3(*j*) and 3(*k*) ($\tau = 36.1$ and 38.9) the turbulent region spreads, involving the entire interfacial region, and in figure 3(*l*) ($\tau = 41.7$) the turbulent region seems fairly uniform in the x-direction. Puffs of the dense, particle-rich, fluid have been ejected into the upper layer, a phenomenon common to many experiments.

A number of distinctive features of the acceleration rotors are to be noted.

(*a*) Their spacing is that of the bottom ripples.

(*b*) They appear at a value of *Ri* when the mean flow, were it not accelerating, is dynamically stable according to Miles–Howard (1964) theory. Dynamical instability is defined as the existence of an exponentially growing root of the linearized equations of motion in the presence of infinitesimal perturbations. Thorpe (1973*a*) found in similar experiments without forcing that mean flow acceleration delayed the onset of dynamical instability to lower *Ri* than expected, owing to the time needed for perturbations to grow to finite size.

(*c*) Their growth is quite slow. The acceleration rotors grow to full size in non-dimensional time $\Delta\tau \approx 11$ while a Kelvin–Helmholtz vortex (figure 5) grows to the same size in $\Delta\tau \approx 4$.

(*d*) If one scales typical velocities from the streaks at the periphery of an acceleration rotor, a given particle completes 3 to 5 circuits over the time that elapses between the appearance of the acceleration rotors and the onset of three-dimensional turbulence.

(e) Streamlines, as indicated by particle streaks, are phase-shifted from the bottom to the interface, indicating an upward flux of horizontal momentum there, and in the absence of significant dissipation indicating that the interfacial waves are time dependent. One can view this momentum flux as additional drag on the flow due to the corrugations in the bottom. The growing interfacial waves are thus 'wave drag' felt by the bottom.

The growth rate in dynamical shear instability depends upon the magnitude of the mean shear rather than on the acceleration. Experiments VI a and V were contrived to determine whether the acceleration rotor is such an instability.

In experiment VI a the tank remains tilted to create a constant-acceleration shear flow. By contrast, the tank is righted in experiment V to remove mean-flow acceleration. Photographs of experiment V are shown in figure 4. The tank is righted in figure 4(*c*), just before the Richardson number drops below 0.25. According to Miles–Howard theory, the flow is unconditionally stable to infinitesimal perturbations. Were this a dynamical instability caused by a finite-amplitude perturbation, the acceleration rotor would continue to grow at the same rate as just before the tank was righted, and this should be the same rate as for experiment VI a.

A comparison of the two experiments is shown in figure 5. Here the first data point of experiment V corresponds to figure 4(*d*), the first photograph after the tank is righted.

The acceleration rotor does grow, slightly, in figures 4(*d*)–4(*f*) as its phase shift with respect to the bottom decreases. In the next three frames, figures 4(*g*)–4(*i*), it shows no further growth, only an additional slight phase shift. The corresponding growth rate for experiment VI a is much higher although decreasing with time. The last data point plotted for experiment VI a corresponds to the onset of turbulence.

The acceleration rotor occurs in both flows while *Ri* is too high for linear dynamical instability. This suggests that it is not a dynamical instability, but rather a convective one. Once the rotor is set up, its growth rate differs depending on whether or not acceleration is present, in further disagreement with Kelvin–Helmholtz theory.

The acceleration rotor is not a candidate for Holmboe instability since there is not the necessary wide separation of velocity- and density-gradient lengthscales at the interface. In a tilting tank in the absence of viscous dissipation, density and velocity

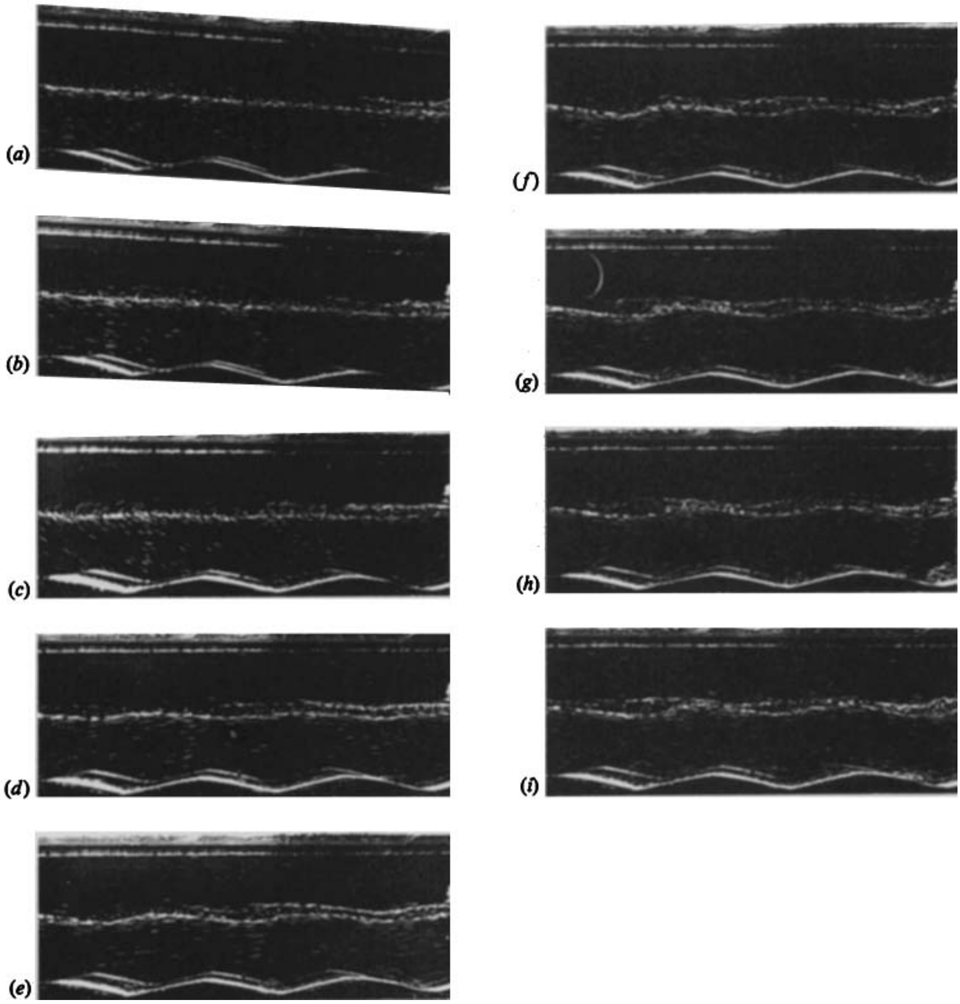

FIGURE 4. Experiment V. Pictures, with exposure times of approximately 0.14 s, are taken at τ (Ri) of (*a*) 18.551 (0.36), (*b*) 20.932 (0.29), (*c*) 23.716 (0.29), (*d*) 26.126 (0.29), (*e*) 28.909 (0.29), (*f*) 31.331 (0.26), (*g*) 33.759 (0.27), (*h*) 36.181 (0.25), (*i*) 38.591 (0.27).

profiles are geometrically similar. If one includes viscosity, there is a possibility that the velocity lengthscale will be greater than that of the density. Thorpe (1973*a*) examines this in detail and gives an expression for calculating the disparity of lengthscales with time:

$$Q = \frac{2}{1+[1+8\beta(\nu t)^{\frac{1}{2}}/\pi]^{\frac{1}{2}}}, \tag{1}$$

where Q is the ratio of density- to velocity-gradient lengthscales, the density gradient goes like $\operatorname{erf}\beta(z-z_0)$, ν is the dynamic viscosity, and t is time. Using typical values for interface thickness, O(3 cm), and elapsed time of experiment, O(15 s), one arrives at an estimate of Q of 0.9. This can be confirmed in the photographs, where no velocity gradient is apparent outside of the density gradient region.

For comparison with acceleration rotor/secondary vortex behaviour, an experiment where Kelvin–Helmholtz instability dominates, experiment IX, is shown in

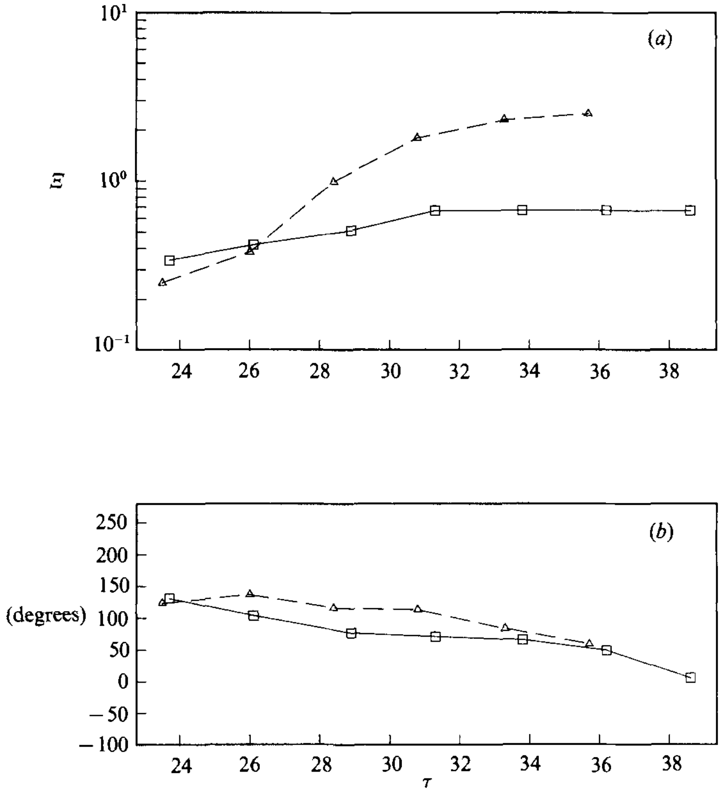

FIGURE 5. Experiment V (□) *vs.* experiment VIa (△). (*a*) Amplitude; (*b*) phase.

figure 6. Note that from figures 6(*c*) to 6(*d*), the right-hand billow has moved by approximately its own diameter, 8.5 cm, to the left. Using the mean measured values of U_1 and U_2 between the frames, Kelvin–Helmholtz theory predicts a phase speed of -8.58 cm s^{-1}, or a displacement of 8.9 cm to the left. Further, the spacing of the billows bears no relationship to the bottom, but rather to that predicted by Miles–Howard theory. Miles & Howard (1964) predict a most unstable wavenumber of $7.57\delta_u$, where δ_u is the shear-layer thickness. For an interface thickness of 2.8 cm, as in this experiment, the spacing should be 20.4 cm. The spacing between billows in figure 6(*d*) varies from 21.4 to 25.5 cm.

In the next section, we shall develop a linear analytical model that exhibits the behaviour of the acceleration rotor. Following that the model will be compared to experiments.

3. A linear model

Assume an infinitely long tank having a frame of reference anchored to the bottom with the x-direction to the right and z upwards as shown in figure 2. The lower and upper layers are labelled 1 and 2 respectively. Mean layer thickness and mean-flow velocity of the lower/upper layers are h_1/h_2 and U_1/U_2 respectively. Total tank depth is h. The ratio of layer thicknesses is given by the parameter

$$\gamma \equiv h_2/h_1. \tag{2}$$

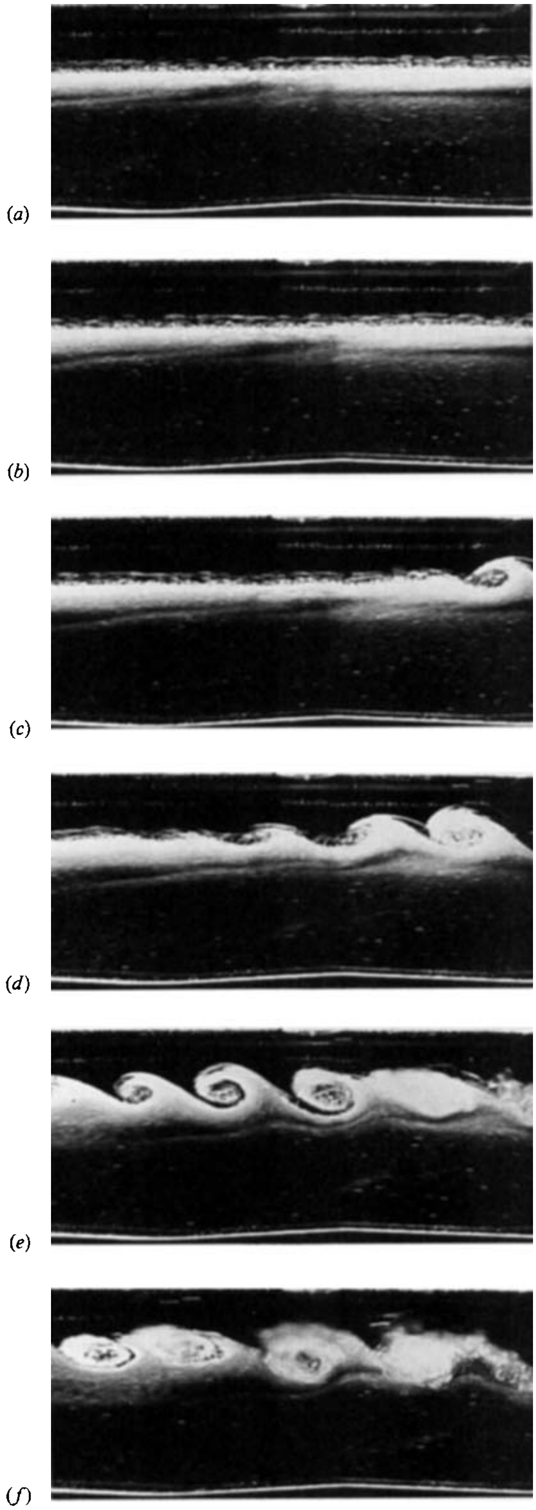

FIGURE 6. Experiment IX. Pictures, with exposure times of approximately 0.12 s, are taken at τ (Ri) of (*a*) 16.635 (0.22), (*b*) 18.487 (0.18), (*c*) 20.331 (0.14), (*d*) 22.147 (0.12), (*e*) 23.992 (0.10), (*f*) 25.843 (0.09).

The flow within each layer is assumed to be two-dimensional and irrotational. So, the linearized, inviscid, Boussinesq equations of motion can then be written in terms of velocity potential φ as

$$\varphi_{jtx}+U_j\varphi_{jxx}=\frac{-\pi_{jx}}{\rho_j} \quad \text{for } j=1,2, \tag{3a, b}$$

$$\varphi_{jtz}+U_j\varphi_{jxz}=\frac{-\pi_{jz}}{\rho_j} \quad j=1,2, \qquad 4a,\, b)$$

$$\varphi_{jxx}+\varphi_{jzz}=0 \quad j=1,2. \tag{5a, b}$$

Here, ρ is density, t is time and subscripts t, x and z denote partial differentiation. Pressure π has been redefined to incorporate hydrostatic terms:

$$\pi_j \equiv p_j-\rho_j g(z-h) \quad \text{for } j=1,2, \tag{6}$$

where p is static pressure and g the gravitational acceleration.

Boundary conditions are that there is no flow through the top, bottom or interface, and that pressure must match at the interface. Hence

$$\varphi_{2z}=0, \quad z=0, \tag{7}$$

$$U_1\eta_x=\varphi_{1z}, \quad z=0, \tag{8}$$

$$\zeta_t+U_j\zeta_x=\varphi_{jz}, \quad z=h_1 \quad \text{for } j=1,2, \tag{9a, b}$$

$$p_1=p_2, \quad z=h_1 \tag{10}$$

where $\eta(x)$ defines the bottom boundary and $\zeta(x,t)$ the interface.

Bottom topography is described by $\eta=\eta_0\,\mathrm{e}^{ikx}$. We non-dimensionalize by scaling x wth k, z with h_1^{-1}, and time with $(kg')^{\frac{1}{2}}$, where g' is the reduced gravity

$$g' \equiv \frac{g(\rho_1-\rho_2)}{\rho_1}. \tag{11}$$

Further, we introduce the phase speed of interfacial free waves in infinite-depth fluid in the absence of shear $c_0 \equiv (g'/k)^{\frac{1}{2}}$, the steepness of bottom forcing $\sigma \equiv \eta_0 k$, the scaled lower-layer depth $\delta \equiv kh_1$, the non-dimensional time τ, the non-dimensional interface perturbation amplitude ξ, and the mean flow Froude number for each layer $F_j \equiv U_j/c_0$. Equations (3)–(10) then can be written in terms of the non-dimensional velocity potential ϕ, as

$$\delta^2\phi_{jXX}+\phi_{jZZ}=0 \quad \text{for } j=1,2, \tag{12a, b}$$

$$\phi_{2Z}=0, \quad Z=1+\gamma, \tag{13}$$

$$\mathrm{i}\sigma F_j\,\mathrm{e}^{\mathrm{i}X}=\phi_{1Z}, \quad Z=0, \tag{14}$$

$$\xi_\tau+F_j\xi_X=\delta^{-1}\phi_{jZ}, \quad Z=1 \quad \text{for } j=1,2, \tag{15a, b}$$

and

$$(\phi_1-\phi_2)_\tau+F_1\phi_{1X}-F_2\phi_{2X}+\xi=0, \quad Z=1. \tag{16}$$

Note that the momentum equations (3) and (4) and the dynamic boundary condition (10) have been incorporated into (16).

A single-mode solution and separation of variables are now imposed. Equations (12)–(16) admit the solution

$$\phi_1=[\Phi_1(\tau)\cosh\delta Z+\mathrm{i}\sigma F_1\sinh\delta Z]\,\mathrm{e}^{\mathrm{i}X}, \tag{17}$$

$$\phi_2=\Phi_2(\tau)\cosh\delta(Z-1-\gamma)\,\mathrm{e}^{\mathrm{i}X}, \tag{18}$$

$$\xi=\Xi(\tau)\,\mathrm{e}^{\mathrm{i}X}. \tag{19}$$

The problem becomes that of solving for the coefficients Φ_1, Φ_2 and Ξ. After some algebra, it can be reduced to a single second-order ordinary differential equation describing the time evolution of the interface,

$$\ddot{\Xi}+\mathrm{i}2\beta\kappa F_1\dot{\Xi}+\beta[1-\mu F_1^2+\mathrm{i}\kappa\dot{F}_1]\,\Xi=\frac{\beta\sigma}{S_1}[\mathrm{i}\dot{F}_1-F_1^2]. \tag{20}$$

Here, we have introduced the notation

$$S_1\equiv\sinh\delta,\quad \beta\equiv[\coth\delta+\coth(\delta\gamma)]^{-1},$$

$$\kappa\equiv\coth\delta-\gamma^{-1}\coth(\delta\gamma),\quad \mu\equiv\coth\delta+\gamma^{-2}\coth(\delta\gamma),$$

and $\mathrm{d}/\mathrm{d}\tau\{\ \}=\{\dot{\ }\}$. We have also used the fact that mass is conserved in the sealed tank,

$$F_1=-\gamma F_2. \tag{21}$$

Finally, the equation is transformed into a (accelerating) frame of reference travelling at the mean velocity of the two layers,

$$a=\Xi\exp\left[-\mathrm{i}\beta\kappa\int_0^\tau F_1(\tau_*)\,\mathrm{d}\tau_*\right], \tag{22}$$

to yield

$$\ddot{a}+\beta[1-[\mu-\beta\kappa^2]\,F_1^2]\,a=\frac{-\beta\sigma}{S_1}[\mathrm{i}\dot{F}_1-F_1^2]\exp\left[-\mathrm{i}\beta\kappa\int_0^\tau F_1(\tau_*)\,\mathrm{d}\tau_*\right]. \tag{23}$$

This is a forced Schrödinger equation. For $\dot{F}_1$ constant analytic solutions exist as parabolic cylinder functions as noted by Thorpe (1969). For arbitrary $\dot{F}_1$ the equation is integrated numerically using the variable step algorithm of Bulirsch & Stöer (1966). A stream function, for contouring, is then derived from the numerical results.

A number of features of the dynamics are now apparent. For

$$F_1\leqslant[\mu-\beta\kappa^2]^{-\frac{1}{2}}, \tag{24}$$

the solution takes the form of two interfacial free waves travelling with the (instantaneous) phase speed

$$C_\pm=\beta^{\frac{1}{2}}[1-(\mu-\beta\kappa^2)\,F_1^2]^{\frac{1}{2}}. \tag{25}$$

The point

$$F_1=[\mu-\beta\kappa^2]^{-\frac{1}{2}}, \tag{26}$$

where the homogeneous equation becomes elliptic, is the point of Kelvin–Helmholtz instability. Also, for $\sigma>0$ there is a resonant forcing of one of the interfacial free waves by the bottom when

$$F_1=\mu^{-\frac{1}{2}}. \tag{27}$$

If $\gamma=1$, the resonant forcing and the Kelvin–Helmholtz instability coincide. Otherwise, the forced resonance precedes the instability for F_1 increasing. In this case, the resonance point divides the hydraulically 'subcritical' regime, where interfacial waves travel in both directions with respect to the bottom, from the 'supercritical' one.

For non-accelerating flow, the governing equation is (20) with $\ddot{\Xi}$, $\dot{\Xi}$ and $\dot{F}_1$ equal to 0. For the 'subcritical' case the interface is 180° out of phase with the bottom. Streamlines within the lower layer are 180° out of phase with the interface and have amplitudes increasing monotonically with height from negative near the bottom to positive near the interface.

For accelerating flow, the coefficient of the forcing term in (22) has a complex amplitude. It is this phase shift that allows formation of closed-streamline regions, the acceleration rotors, in the solution.

In physical terms, the lower-layer flow over sinusoidal bottom ripples sets up evanescent internal waves there. These force the two sinusoidal interfacial free waves which add to form a standing wave. In a steady mean flow the equilibrium amplitude of the interface would be determined by the flow's proximity to the point of resonant forcing, owing to mean flow acceleration, however, the wave does not achieve its equilibrium amplitude. As a result it is phase-shifted from the bottom, allowing a net vertical energy flux. The passage of energy through the evanescent region into the interfacial wave is analogous to 'tunnelling' in quantum mechanics.

Thus, for accelerating flow, streamlines in the lower layer have a depth-dependent phase shift within the layer. As the interfacial wave grows, streamline amplitudes change correspondingly. But, so long as the interfacial wave is not at equilibrium amplitude, it maintains a phase shift with respect to the bottom.

The interfacial wave in turn forces evanescent internal waves in the upper layer. Since there is no sink for their energy, these waves exhibit no 'tunnelling' and their streamlines have an attenuating amplitude but no depth-dependent phase shift within the layer.

Another physical mechanism analogous to mean-flow acceleration in forming rotors in this model would be linear friction within each layer. In this case, it would be the need for the interface to remain at constant amplitude in the presence of dissipation that would require a net energy flux from the bottom. There were no significant frictional effects observed away from the boundaries in the experiments.

4. Comparison with experiments

For subsequent analysis, data are obtained from the photographs as follows. The interface is defined to be the centre of the region of no motion in the unperturbed shear flow. The level of the interface can be read within ± 2 mm. Amplitudes of the interfacial perturbations are measured directly from the photos, where possible, reflecting the position of the interface as just defined. In cases where the interface is obscure, measurements are taken at the top of the dense layer of streaks. Phase measurements are taken by determining, by eye, the best fit to the interface of a sinusoid of the amplitude and wavelength of the bottom. Phase is defined as positive in the upstream direction of the lower layer. Although more precise methods of fit exist, this one proved very easy to implement and quite satisfactory, albeit with large error bars for low-amplitude or double-vortex photos.

For all of the experiments of table 1, the analytical model was numerically integrated from near-zero initial conditions with the measured experimental parameters. The model's behaviour is not sensitive to perturbations in the initial conditions.

When started from zero, a time offset of the model's interface growth from the experiments is observed. This is due presumably to the combined effects of tilting accelerations, finite tank length, flow separation from the bottom, and non-zero interface thickness, none of which are included in the model. The mean time offset is 4.56 ± 1.80 (one standard deviation) in τ. Where noted, results have been corrected for this mean offset.

Once the model is started, output is obtained at times corresponding to the midpoint of each exposure. The stream function is calculated and contoured at equally spaced levels, the same for all plots. The calculated stream-function field is 100 by 100 points; plot features smaller than the point spacing are artifacts of the contouring routine.

A comparison of the analytical model, corrected for time offset, with experiment II is shown in figure 7. In figure 7(*c*) the recirculating region appears in the model. The exact time of its appearance is determined by the contour intervals selected. By figure 7(*d*), the model is beginning to fail. The experiment shows a marked 'cuspiness' in the interface. The model, however, is constrained to a sinusoidal interface. As a consequence, non-physical jets are beginning to appear in the region of the acceleration rotor. Cuspiness does appear in interior streamlines of the lower layer and is due there to the sum of the linear perturbation field with the mean flow. Note that streamlines near the interface show a tendency to shorten the leading edge of the sinusoid, where the acceleration rotor occurs, in agreement with the experiments. This asymmetry is pronounced in the next frame. Separation of the flow from the bottom as well as the thinning of the interface are not reflected in such a simple model, yet the phase shift of the interface with respect to the bottom is clear.

By figure 7(*e*), the model is diverging from the experiment, presumably due to lack of harmonics in the assumed form of the solution. No trace of the secondary vortices ever appears.

Model behaviour is compared quantitatively with this experiment in figure 8. No time-offset correction has been applied. Although this is one of the poorest matches between the model and an experiment, agreement is still good.

The model was run for all experiments in which the acceleration rotor evolved clearly in a constant-acceleration mean flow. For each experiment, initial interfacial wave growth rate is calculated from both the data and the model runs. Growth rate from the data is the average growth in amplitude over the first two data points. Growth rate from the model is the average for the model at amplitudes corresponding to the same two data points. It should be noted that, despite mean-flow acceleration, initial growth rate was essentially constant for the data and only changed gradually for the model. Figure 9 compares the growth rate from the model against that from the data. The straight line indicates a perfect fit. Four of the predicted growth rates did not match well for reasons that are not clear. The worst match is the case of figure 7, so it is safe to conclude that the numerical model does a good job of predicting the initial growth of the acceleration rotor.

When tilt is removed from the numerical model, the flow relaxes towards the steady-state solution. If the flow is in the Kelvin–Helmholtz regime, the interface amplitude continues to grow, with interface phase reflecting advection of the waves by the mean flow. Otherwise it finds a non-growing configuration, in agreement with experiment V.

Since the model is incapable of reproducing the secondary vortex, an additional series of experiments was performed to understand its origin. Experiment XI, shown in figure 10, was contrived to show the flow of the intermediate-density water at the interface. To this end, the interface was dyed white.

Figure 10(*d*) shows clear evidence of overturn in the acceleration-rotor region, both by the streaks (indicating instantaneous velocity) and the dye (indicating integrated velocity). Note that the acceleration rotors are mainly entraining intermediate-density water. Figure 10(*f*) shows fully developed acceleration rotors as well as the resultant thinning of the 'braid' region connecting them. Figure 10(*g*) shows the emergence of the secondary vortices spaced half-way between the

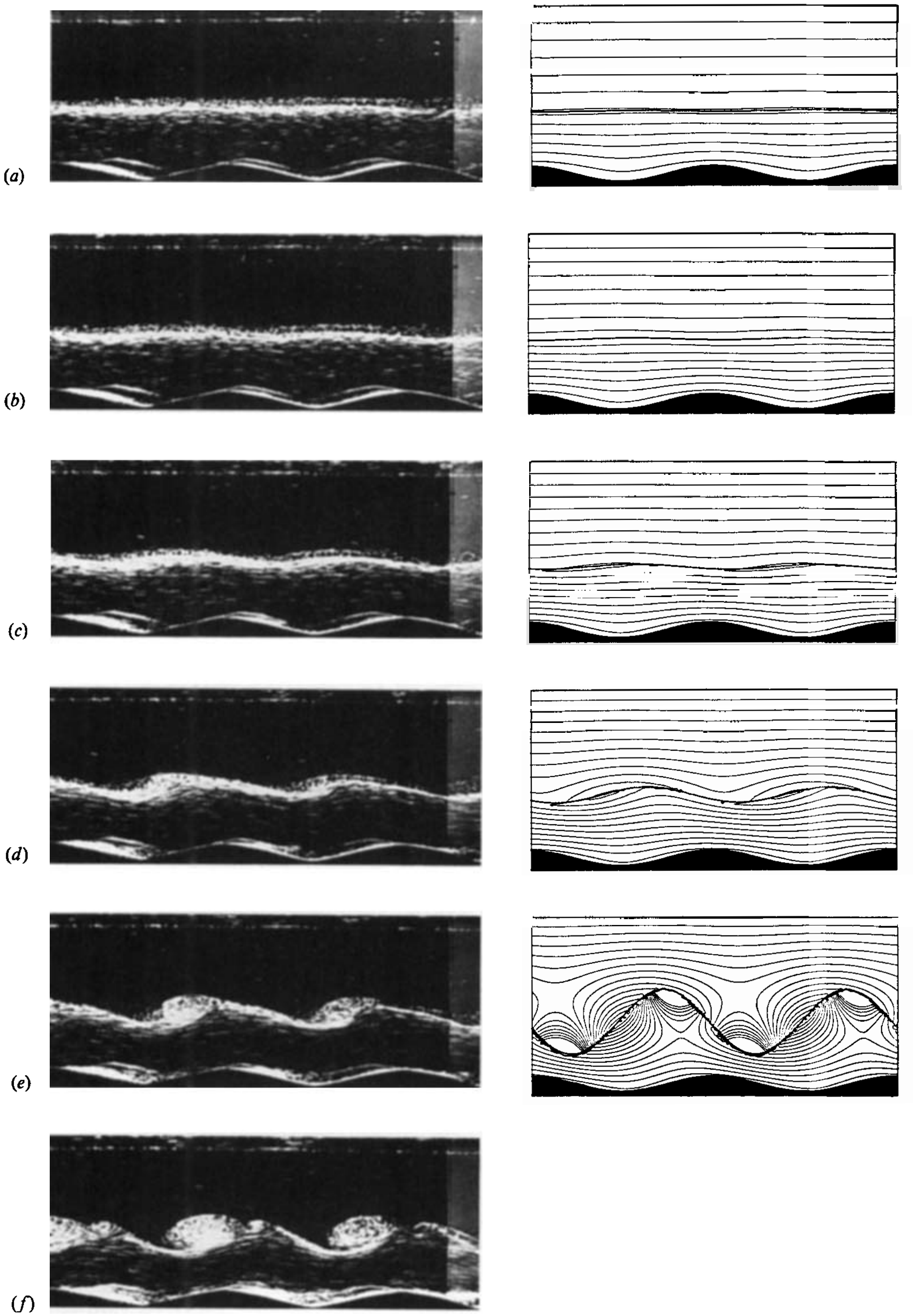

FIGURE 7. Experiment II compared with the linear model. The total stream function is contoured. Pictures, with exposure times of approximately 0.25 s, are taken at τ of (*a*) 17.743, (*b*) 20.519, (*c*) 23.280, (*d*) 26.071, (*e*) 28.828, (*f*) 31.584.

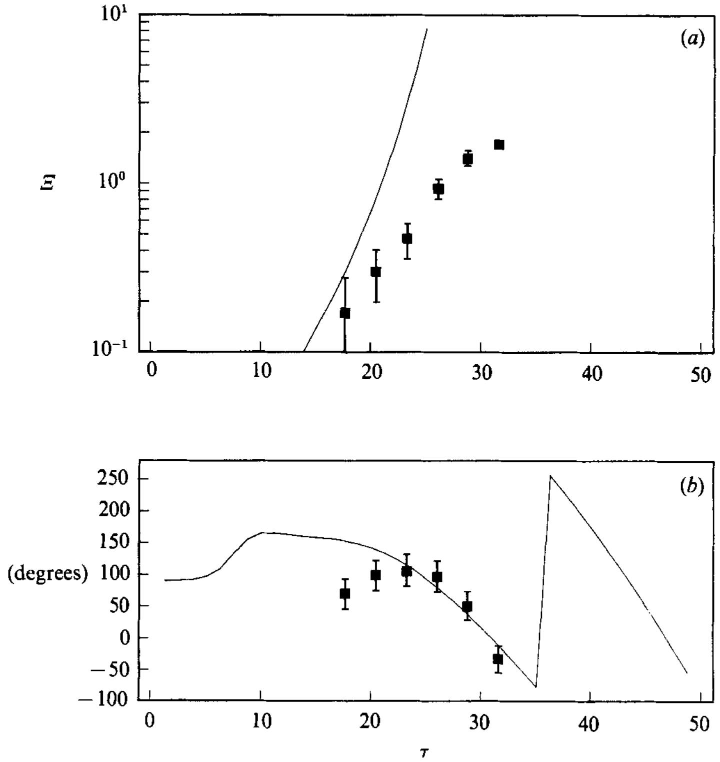

FIGURE 8. Experiment II compared with the single-mode linear model. (*a*) Amplitude; (*b*) phase.

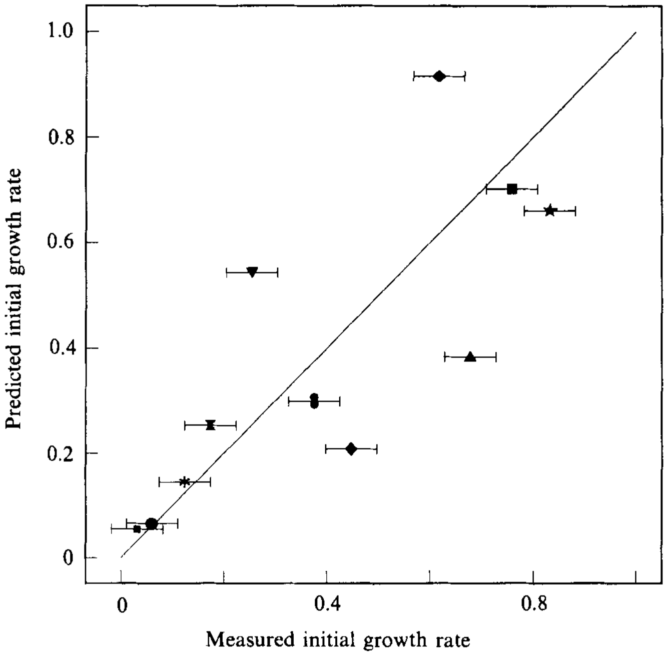

FIGURE 9. Initial growth rate predicted by the linear model *vs.* measured initial growth rate. Points correspond to experiments: ▼, I; ◆, II; ⧗, III; ⦂, IV; ★, V; ■, VIa; ▲, VIIa; ♦, VIIIa; ✱, XI; ■, XII; ●, XIII.

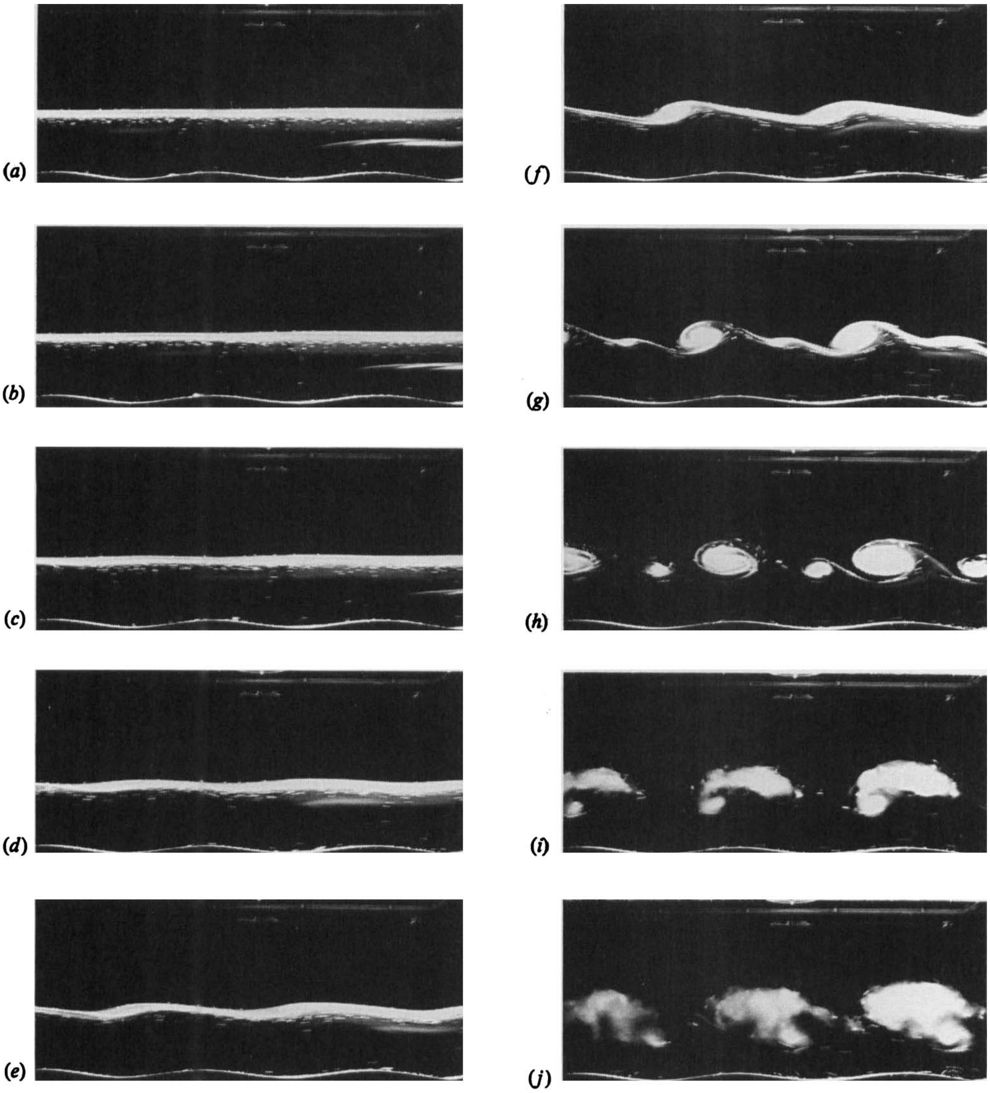

FIGURE 10. Experiment XI. Pictures, taken with exposure times of approximately 0.12 s, are taken at τ (Ri) of (*a*) 15.939 (0.37), (*b*) 18.593 (0.31), (*c*) 21.908 (0.26), (*d*) 24.557 (0.22), (*e*) 27.197 (0.18), (*f*) 29.850 (0.14), (*g*) 32.499 (0.11), (*h*) 34.485 (N/A), (*i*) 37.181 (N/A), (*j*) 39.843 (N/A).

acceleration rotors. The secondary vortices entrain the remainder of the dyed fluid, thinning the interface further. Figure 10(*h*) shows both sets of vortices grown to full size. Note that the secondary vortices have grown more rapidly than the primaries in figures 10(*e*)–10(*h*). Also, while equally spaced in figure 10(*g*), the secondaries, by figure 10(*h*), have moved to the right with respect to the primaries. This movement corresponds to a mean phase speed of 4.33 cm s^{-1}; the Kelvin–Helmholtz dispersion relation predicts 4.12 cm s^{-1}. The acceleration rotors move at about half this speed.

Using the undisturbed interface thickness and measurements from photos, the Miles–Howard criterion predicts a most-unstable wavelength of 13.5 cm at the time of figure 10(*f*). The mean-flow Richardson number in figure 10(*g*), where the

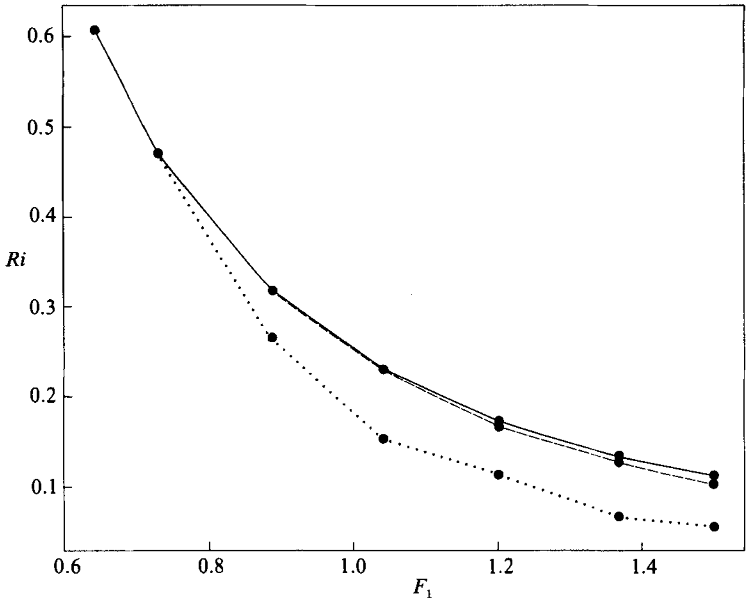

FIGURE 11. Experiment II, Richardson number *vs.* lower-layer Froude number (proportional to time). The solid line is calculated using the initial interface thickness. The dotted line is calculated using the interface thickness measured between acceleration rotors. The dashed line is calculated assuming uniform thinning of the interface.

secondary vortices first appear, is 0.08 when one allows for thinning of the interface as in figure 11. Thorpe (1973*a*) examines vortex spacing *vs.* Richardson number for Kelvin–Helmholtz vortices. His figure 3 shows that for $Ri = 0.08$ the mean value of s is 0.48 ± 0.04, where s is defined as the ratio of maximum billow height to disturbance wavelength. The height of the fully-developed billows of figure 10(*h*) is about 6.25 cm, yielding $s = 0.46$, in agreement with Thorpe's findings.

Thus, the secondary vortices, by their higher growth rate, by their phase speed, and by their ratio of maximum diameter to most-unstable wavenumber are consistent with Kelvin–Helmholtz billows. The degree of thinning of the interface braid region is shown in figure 11, based on the data of experiment II. Three lines are plotted. The solid line is the estimated mean-flow Richardson number using a linear gradient approximation for velocity and density across the interface,

$$Ri \equiv \frac{N^2}{\left[\dfrac{\mathrm{d}U}{\mathrm{d}z}\right]^2} = \frac{k\gamma^2 T_i}{F_l^2[\gamma+1]^2}, \tag{28}$$

where F_l is obtained by the velocity measurements outlined in the Appendix and T_i is the thickness of the unperturbed interface. The dotted line is Ri based on the measured local interface thickness, T_l, in the thinned region between acceleration rotors, rather than on T_i. The dashed line is Ri calculated assuming a uniform thinning of T_i by stretching it into a sinusoid of the measured perturbation amplitude. Note that there has been a significant local reduction in Ri due to the thinning of the interface by the acceleration rotors.

In his study of Woods' 1968 photos, Thorpe (1973*b*) suggests that secondary shear instabilities often occur at the crest or trough of the primary wave, where the total shear is a maximum. This is the case in experiments I–VII, having high-amplitude

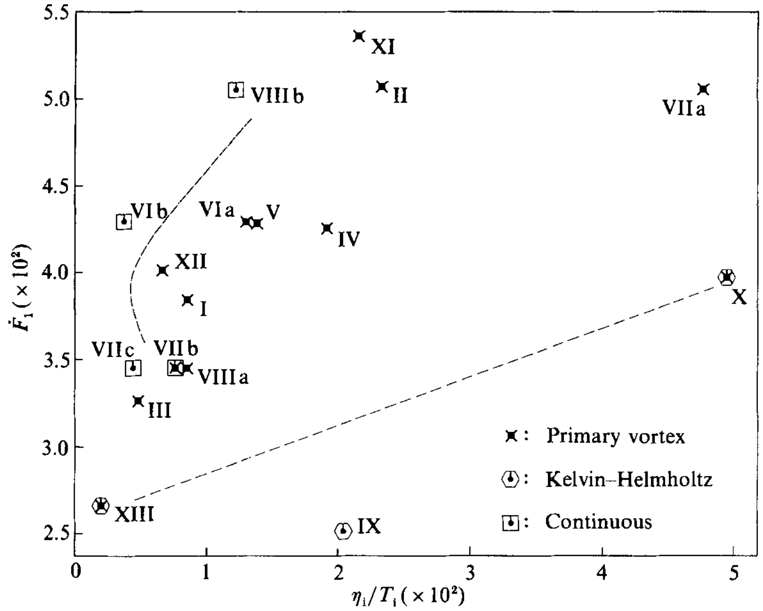

FIGURE 12. The distribution of phenomena for all two-layer experiments. The ordinate is the acceleration of the mean flow. The abscissa is a ratio of forcing amplitude (η_i) to interface thickness (T_i).

forcing. However, the appearance of the billow in the minimum-shear area of experiment XI suggests thinning of the interface as the dominant mechanism for local *Ri* reduction in this case. The interaction of the acceleration rotors and secondary vortices agrees qualitatively with the numerical calculations of Chow (1979, figure 4.3.2), which is a study of the interactions of adjacent Kelvin–Helmholtz vortices.

The question of when one expects to see the acceleration rotor remains. Figure 12 summarizes the results of the experiments. The phenomena observed are broken down into three classes: Kelvin–Helmholtz-like, acceleration rotor, and continuous. The latter refers to the critical layer in a constant-buoyancy fluid as examined by Thorpe (1981).

The horizontal axis of this figure is contrived to give some measure of the thickness of the interface region. The initial interface thickness, T_i, is normalized by the amplitude of the wave generated by the bottom forcing, η_i, exponentially attenuated to the value felt at the unperturbed interface, $\eta_i \equiv \eta_0 \, e^{-\delta}$. Thus, moving to the left on this axis indicates interface thickness increasing compared with the amplitude of internal wave forcing. Moving upwards on the vertical axis indicates increasing mean-flow acceleration.

Three tentative regimes emerge from this figure. The region in which the acceleration rotor dominates is bounded to the left by the 'continuous' region; for a given value of $\dot{F}_1$, as the interface thickens the critical layer eventually behaves as if it is embedded in a constant-buoyancy region. The 'continuous' region curves over the acceleration rotor region, an unexpected result which bears further study.

The region below the acceleration rotor regime is dominated by Kelvin–Helmholtz instability. Decreasing $\dot{F}_1$ for a given η_i/T_i decreases the amplitude of the forcing term in (23), allowing Kelvin–Helmholtz instability to dominate. This boundary is quite tentative but appears to rise with increasing η_i/T_i.

5. Conclusions

This work has examined a new scenario for instability, the acceleration rotor, occurring at the critical layer in accelerating two-layer flows. It is characterized by a rotor region at the interface that extracts energy from the incident internal wave field and stays approximately phase-locked to that field. The acceleration rotor can occur at mean-flow Richardson numbers of order 0.5. Acceleration as well as shear are necessary for its initiation. However, once the rotor is initiated, it appears to be quasi-stable when acceleration is removed.

The acceleration rotor can be analytically modelled by a linear, inviscid, irrotational, two-layer, single-mode system. Such a model, while by no means complete, is in good qualitative agreement with observed amplitudes, phases, and growth rates of the acceleration rotor in its early stages. Later development of the acceleration rotor, as well as secondary shear instabilities, depend on higher-order terms in the momentum equations than are included here.

Secondary vortices arising in some experiments appear to be Miles–Howard-type shear instabilities. Their location in the flow is the result of a trade-off of mechanisms that cause a local reduction in Ri. Two mechanisms identified here are modulation of the mean shear by the interfacial waves and local thinning of the interface due to fluid entrainment by the acceleration rotor.

An image processing system which allows for the automatic reading of streaks from photographs has been used to obtain velocity measurements. The system is designed to use standard low-cost hardware. The software is designed to be portable, being written in Fortran 77. It is menu-driven, highly modular, and easily modified. Velocity measurements of modest accuracy (±10%) can be obtained from a photograph in roughly one hour of operator time.

The author gratefully acknowledges the help of R. E. Hall, W. K. Melville, and J. W. Miles. Many helpful suggestions were made by anonymous reviewers. Plotting software was provided by R. L. Parker. Illustrations were prepared with the help of D. Betts, W. Call, D. Menegus and P. M. Kimber. This work was supported by N. S. F. grants OCE 80-09461, OCE 81-17539, and OCE 82-40404. Support during manuscript preparation was by NSERC and INO.

Appendix. Velocity measurements

An automated system for reading particle-streak photographs, developed as part of this work, was used on a representative photograph to obtain velocity measurements within the critical layer. Since the first-order behaviour of the acceleration rotor turned out to be explicable by other measurements, these velocity measurements were used only for the Richardson-number values of figure 11.

A typical photo, frame 12 of experiment VIa, is shown in figure 13. It was chosen for the range of streak density: relatively high at the interface, moderate in the lower layer and sparse in the upper layer. Also, the lower-layer streaks in the central illuminated strip are noticeably brighter than those closer to the camera or farther from it. Visible in the photo are six small cross-shaped black marks on white background, applied to the rear glass of the tank in three equally spaced vertical columns. Six corresponding marks are barely visible on the front glass of the tank. These are 'fiducial marks', used to register the image coordinate system to 'real world' coordinates and to check the accuracy of geometrical corrections.

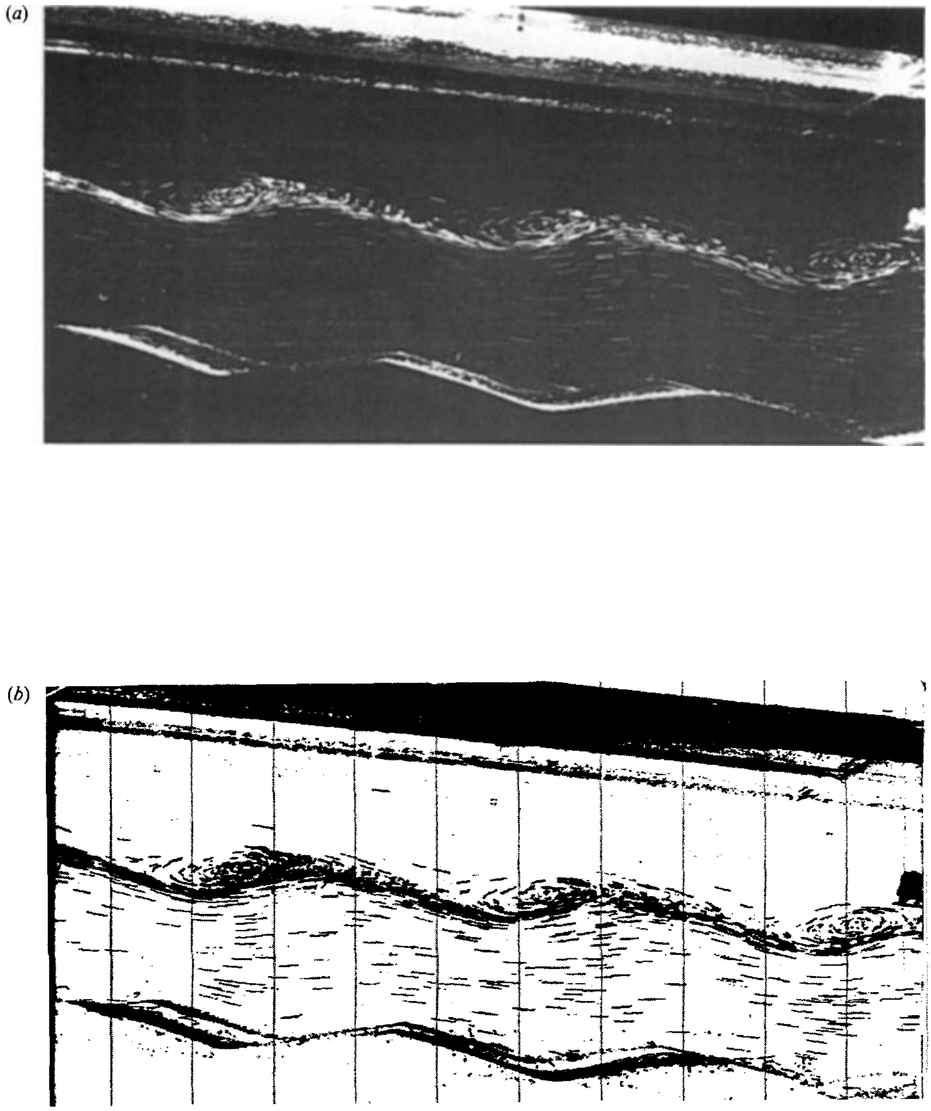

FIGURE 13. A frame of experiment VIa. (*a*) As photographed, (*b*) digitized to 1060 × 512 pixels and displayed as a two-toned plot.

The digitized image displayed in a two-tone plot is shown in figure 13(*b*). Note traces of the three upper rear fiducial marks. After simple pixel-level processing; nonlinear intensity mapping, first-differencing, and clipping to positive values, streaks in the interface region emerge. This can be seen in figure 14(*a*). Streaks not in the brightly lit region tend to be broken up by the processing.

At this point, pixels are automatically connected into 'candidate' streaks using a recursive forward–backward table searching algorithm. The reduction in data points by a factor of 10^3 facilitates subsequent processing. Figures 14(*b*) shows the connected candidate streaks of figure 14(*a*) after preliminary filtering. The upper edge of the tank and parts of the rippled bottom are still evident. A number of long streaks at the interface are the result of overlapped streaks in the digitized image.

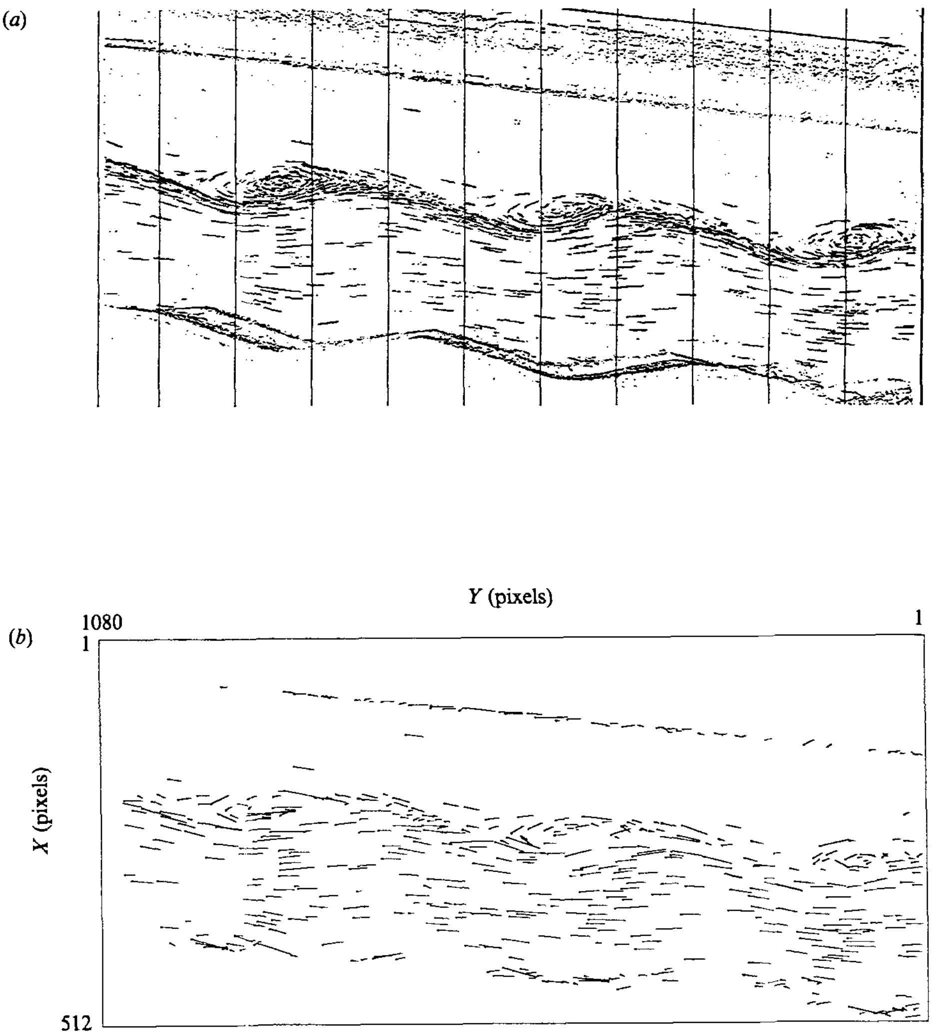

FIGURE 14. (*a*) The image of figure 13(*b*) after pixel-level filtering; (*b*) candidate streaks read from the image.

Some streaks in the lower level have been broken into short segments. These are marginal contrast streaks from outside the illuminated strip.

Next the picture is filtered with an interactive editor. The filtering scheme applied is *ad hoc*, and is an attempt to crudely duplicate human reasoning. Streaks that differ significantly from their neighbours, either in length or direction, are questionable. So, a region is outlined and statistics taken to determine 'typical' streaks within it. Outliers are discarded. In the interface region, streaks much longer than their immediate neighbours are discarded, being most probably overlapped streaks. Between 10 and 20 streaks were 'manually' discarded by comparison of the plot with the photo. The whole interactive process took about one hour real-time and resulted in figure 15(*a*). It must be stressed that although determining suitable statistical filters is a time-consuming step, once performed on one frame of a series it can subsequently be automatically applied to other statistically similar frames, cutting

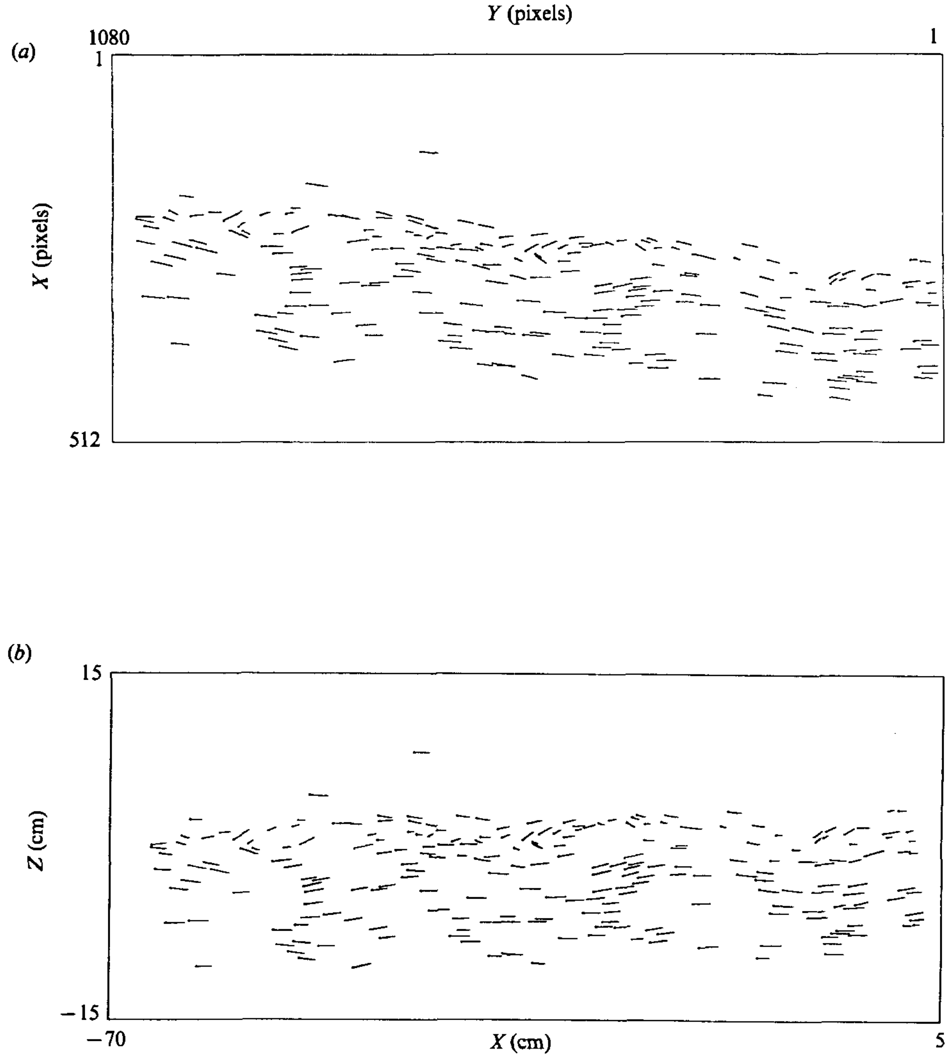

FIGURE 15. (a) Candidate streaks after streak-level filtering; (b) calibrated velocities after geometrical corrections.

down on the time expended per frame. The final 'manual' step of comparison with the photo takes about ten minutes per frame and is optional.

Geometrical corrections are applied to the streaks of figure 15(a) to yield the calibrated velocities of figure 15(b). The lengthscale of velocity has been adjusted to facilitate comparison with the original photo. At this point, an error estimate is made. Subsets of fiducial marks are used to calculate the transformation to real-world coordinates and corrections for refraction and perspective applied to the unused fiducials. The r.m.s. error of location derived when the corrections are applied is 1.7 mm. This is an estimate of all remaining errors and distortions not explicitly corrected. So, the velocity measurements are located within ± 2 mm in x and y. A rough estimate of accuracy of the measurements, obtained from statistical scatter in simpler analytically tractable flows is $\pm 10\%$. The total number of velocity measurements obtained is 229.

REFERENCES

ARMI, L. 1978 Mixing in the deep ocean – the importance of boundaries. *Oceanus* **21**, 14–19.

BROUTMAN, D. 1984 The focusing of short internal waves by an inertial wave. *Geophys. Astrophys. Fluid Dyn.* **30**, 199–225.

BUCKLES, J., HANRATTY, T. J. & ADRIAN, R. J. 1984 Turbulent flow over large amplitude wavy surfaces. *J. Fluid Mech.* **140**, 27–44.

BULIRSCH, R. & STÖER, J. 1966 Numerical treatment of ordinary differential equations by extrapolation methods. *Numer. Math.* **8**, 1–13.

CHOW, C.-Y. 1979 *An Introduction to Computational Fluid Mechanics*. Wiley.

FRITTS, D. C. 1982 The transient critical-level interaction in a Boussinesq fluid. *J. Geophys. Res.* **87C**, 7997–8013.

HAURY, L. R., BRISCOE, M. G. & ORR, M. H. 1979 Tidally generated internal wave packets in Massachusetts bay. *Nature* **278**, 312–317.

KOOP, C. G. & MCGEE, B. 1983 Measurements of internal gravity waves in a stratified shear flow. Preprint – T. R. W. Space & Technology Group, Redondo Beach, CA 90278.

MILES, J. W. & HOWARD, L. N. 1964 Note on a heterogeneous shear flow. *J. Fluid Mech.* **20**, 331–336.

STACEY, M. W. & ZEDEL, L. J. 1986 The time-dependent hydraulic flow and dissipation over the sill of observatory inlet. *J. Phys. Oceanogr.* **16**, 1062–1076.

THORPE, S. A. 1968 A method of producing a shear flow in a stratified fluid. *J. Fluid Mech.* **32**, 293–304.

THORPE, S. A. 1969 Experiments on the instability of stratified shear flows: immiscible fluids. *J. Fluid Mech.* **39**, 25–48.

THORPE, S. A. 1973*a* Experiments on instability and turbulence in a stratified shear flow. *J. Fluid Mech.* **61**, 731–751.

THORPE, S. A. 1973*b* Turbulence in stably stratified fluids: a review of laboratory experiments. *Boundary-Layer Met.* **5**, 95–119.

THORPE, S. A. 1978 On internal waves in an accelerating shear flow. *J, Fluid Mech.* **88**, 623–639.

THORPE, S. A. 1981 An experimental study of critical layers. *J. Fluid Mech.* **103**, 321–344.

ZILKER, D. P. & HANRATTY, T. 1979 Influence of the amplitude of a solid wavy wall on a turbulent flow. *J. Fluid Mech.* **90**, 257–271.